Acta Materialia 258 (2023) 119227

Contents lists available at ScienceDirect

Acta Materialia

journal homepage: www.elsevier.com/locate/actamat

Full length article

Does flash sintering alter the deformation mechanisms of tungsten carbide?

Isacco Mazo [a,*], Miguel A. Monclus [b], Jon M. Molina-Aldareguia [c,b], Vincenzo M. Sglavo [a,d]

[a] Department of Industrial Engineering, University of Trento, Via Sommarive 9, Trento 38123, Italy
[b] IMDEA Materials Institute, C/ Eric Kandel 2, Getafe, Madrid 28906, Spain
[c] Department of Mechanical Engineering, Universidad Politécnica de Madrid, Madrid 28006, Spain
[d] INSTM, Firenze 50121, Italy

ARTICLE INFO

Keywords:
Tungsten carbide
Electric current-assisted sintering (ECAS)
Mechanical properties (high-temperature deformation)
HRTEM
Dislocations

ABSTRACT

The study aims at unravelling the effect of fast and ultrafast electric current-assisted sintering on the plasticity of ultrahard binderless tungsten carbide. The small-scale deformation of polycrystalline micropillars obtained from samples consolidated by Spark Plasma Sintering (SPS) and Electrical Resistance Flash Sintering (ERFS) processes was studied. Micropillars, 3 μm in diameter, were prepared by focused ion beam and compressed ex and in-situ at room and high temperatures (700 °C). Electron-transparent lamellas were milled out from the pillars plastically deformed at different strain levels to carry out Transmission Kikuchi diffraction (TKD) and HRTEM analyses. At room temperature, the micropillars show similar mechanical responses under compression, reaching outstanding yield strengths (8–11 GPa) with plastic strain not exceeding 3–5% because of a dislocation-assisted toughening mechanism. At 700 °C, the pillar's yield strength drops to around 1.5–2 GPa accompanied by the relevant temperature-activated plasticity. However, only the pillars prepared from flash-sintered material can be homogeneously deformed up to ≈50%; conversely, those derived from SPS ceramics fail macroscopically at strains of ≈20–25% strain upon the localisation of plastic strain at shear bands.

1. Introduction

Binderless tungsten carbide (BTC) ceramics have been recently studied as an alternative to the cemented carbide counterpart. The soft and ductile binder phase, usually Co, is an excellent technological solution to resolve, at the same time, the low sinterability and toughness of tungsten carbide [1]. Although the relatively low melting point and limited chemical, oxidation and radiation resistance of the metal phase limit the applicability of cemented carbide (WC/Co, WC/Ni or WC/Fe) components at high temperature and/or in harsh environments, they have found an extensive use as tool inserts, abrasive and wear resistant parts, high pressure nozzles and sealings in many industrial sectors [1,2]. In addition to those critical applications, BTC components are regaining focus from the research community as neutron shielding material in fast breeder reactors [3] and as a promising candidate for plasma-facing components of fusion reactors [4–6]. Despite its intrinsic brittle behaviour, monolithic WC shows unexpectedly higher thermal shock resistance than cermets when subjected to extreme heat flux conditions like edge localisation and plasma disruption events [7]. WC and some of its composites (WC/B_4C, WC/TiC, etc.) also combine neutron reflecting and absorbing capability of heavy (W) and light elements (C or B), possibly outperforming metallic W-based neutron shielding materials [4,5]. In the absence of a metallic binder, two are the main challenges for the successful production of BTC products [8]: (i) obtaining highly dense bodies (98–99%+ relative density) upon sintering and (ii) boosting the inherently low fracture toughness. The extremely limited self-diffusivity of W and C atoms [9] makes pressureless sintering of pure WC powders fairly feasible [10]. Only high pressure-high temperature and fast sintering techniques lead to reasonably good results in terms of density, grain size, phase stability and hardness [11–13]. Out of such techniques, the most promising for consolidating BTC powders is spark plasma sintering (SPS) [14], which allows obtaining fully dense bodies with good control of the final microstructure in terms of grain size and semicarbide (W_2C) formation [15,16]. Typically, BTC products consolidated by SPS achieve 98–99+% density, hardness of about 28–30 GPa and fracture toughness in the range of 4–6 MPa $m^{1/2}$ [16,17], the latter being often too low for most structural applications. Bulk ceramics, BTC components included, are typically characterised by the trade-off relationship between hardness and fracture toughness [17,8]: the harder the material, the less plasticity is available for intrinsic toughening mechanisms [18]. Toughening phenomena can sometimes be activated in BTC using fibers, whiskers or

* Corresponding author.
E-mail addresses: isacco.mazo@unitn.it, isacco.mazo@mines-albi.fr (I. Mazo).

https://doi.org/10.1016/j.actamat.2023.119227
Received 28 March 2023; Received in revised form 7 July 2023; Accepted 6 August 2023
Available online 15 August 2023

nanotubes reinforcement, grains bridging/interlocking, crack deflection in coarse grain or laminated structures, particles dispersion etc. [8]. Certain oxides are used as alternative binders to increase the material toughness up to 8–9 MPa $m^{1/2}$, introducing crack bridging and deflection mechanisms [19]. Nevertheless, dispersing particles and/or second oxide phases modify the material structure inevitably, impairing not only the native WC hardness, with a drop from 30 GPa down to 18–22 GPa, but especially its thermomechanical [6] and thermophysical

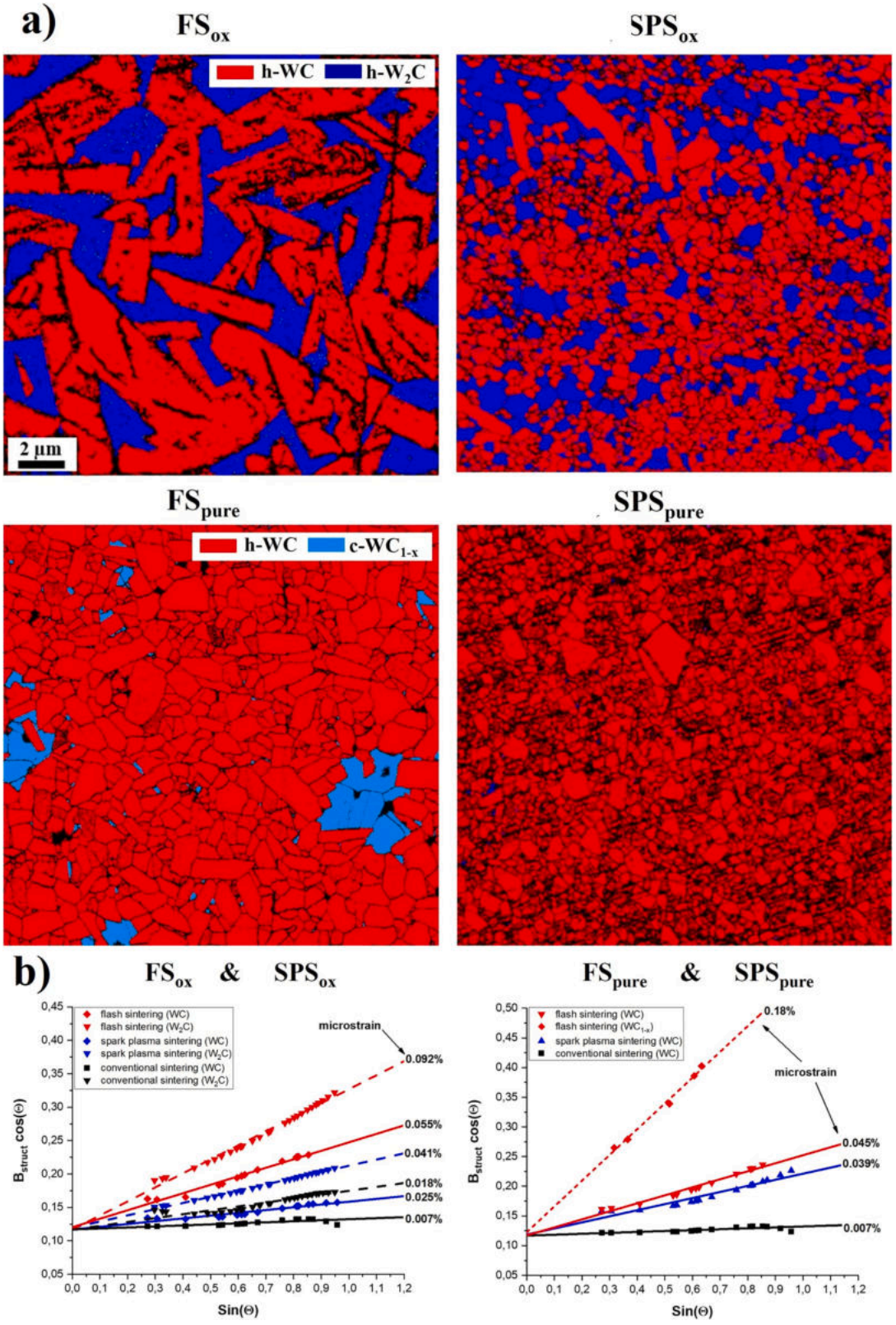

Fig. 1. Electron Backscatter Diffraction (EBSD) (a) and corresponding density of crystalline defects (microstrain) as estimated from X-Ray diffraction for the different phases present (b). Black lines refer to the zero microstrain reference WC sample.

[3] properties. Of critical importance is the anomalous high thermal conductivity of monolithic WC [20] (as high as 100–200 W/m K at room temperature [3,21]), essential for high heat flux applications [3,5,22], which decreases promptly when low thermally conducting ceramics are included [5,23]. Thus, using monolithic BTC for structural components requires new strategies to make this material more damage tolerant, which translates into altering the intrinsic toughening mechanisms of WC [18].

Different deformability has been recently reported for some hard ceramics produced by flash sintering [24]. It was argued that the very high mass transport and flow rate during the flash process accounts for the development of shear stresses at the particles' neck, intense enough to overcome the material yield strength at the high sintering temperature. It was then demonstrated that during flash, the high-temperature deformability is significantly enhanced by the athermal effect, which lowers the activation energy for plastic flow [25].

Although the question about the correlation between the flash event and plastic flow is still under debate within the scientific community [26], "post-flash" dislocations were observed in TiO_2 [27], $Er(Mn,Ti)O_3$ [28] and yttria-stabilised zirconia (YSZ) [29]. In the latter case, shear stresses over 1 GPa were estimated during flash sintering, high enough to allow dislocation pile-up. The copious defects introduced during flash sintering lead to improved plasticity, as reported for YSZ [30], TiO2 [31] and $SrTiO_3$ [32–34]. The application of external electric fields can be used to alter the defect chemistry of oxide ceramics, modifying the oxygen vacancy concentration along grain boundaries [33]. Flash sintering experiments under a direct current (DC) alter the redistribution of oxygen vacancies, promoting their migration towards the negative electrode [32]. This migration was demonstrated to affect the plasticity of $SrTiO_3$ single crystals by favouring the dislocations nucleation over their mobility [34,35]. Within this area of interest, the present work aims at understanding whether flash sintering can also affect the deformability of a non-oxide ceramic, like tungsten carbide (WC). This study wants to disclose if the ultrafast sintering of a non-oxide ceramic promoted by low AC electric fields (~ 5 V/cm) has a role in activating dislocation-induced plasticity at room and high temperatures.

2. Experimental

2.1. Samples preparation

The objective was to investigate the distinctions in the micron-scale mechanical properties of materials consolidated by electrical resistance flash sintering (ERFS), identified as ultrafast sintering, and spark plasma sintering (SPS), referred to as fast sintering. Two different WC nanopowders (Inframat Advanced Materials®) were selected for producing the samples. The powders, as already reported in [36], are characterised by different oxygen content, 1.21 wt% and 0.28 wt% for the oxidised (WC_{ox}) and pure one (WC_{pure}), respectively. Ultrafast (ERFS) and fast (SPS) sintering of said powders produced four different monolithic WC materials, characterised by different phase composition (Fig. 1(a)). Sintering of oxidised nanopowders produced biphasic composites (WC/W_2C = 60/40 vol%) [36]. Conversely, single phase material and metastable cubic WC_{1-x} phase embedded in WC matrix were obtained from the WC_{pure} powder by SPS and ERFS, respectively. Accordingly, the specimens prepared in the present work were labelled as FS_{ox}, SPS_{ox}, FS_{pure} and SPS_{pure} (Fig. 1), where FS is simply referring to the ERFS process. The ERFS process and details on the composition and microstructure of the obtained materials have been previously reported [36–38]. This process consists in the application of small AC voltage (3–4 V) and large current (1000–1200 A) for a duration between 10 s and 60 s, to a powder compact thermally and electrically insulated within a zirconia die. The SPS samples were consolidated by Dr. Sinter 1050 apparatus at K4Sint Srl (Pergine Valsugana, Italy); 20 g of powder were poured in a 20 mm diameter graphite die and sintered at 2100 °C for 5 min under 60 MPa uniaxial pressure, using a heating rate of 200 °C/min.

2.2. Microstructure analysis

The sintered cylindrical pellets were cut along the longitudinal axis, in the direction of the applied electric current and pressure, and polished with diamond abrasive pastes up to a mirror-like surface (1 μm size). The polished surfaces were analysed by EBSD within a FEG-SEM microscope (ThermoFischer® Apreo 2S LoVac). The density of crystalline defects was estimated for the four sintered samples by X-Ray diffraction using PANalytical EMPYREAN diffractometer, with Cu-Kα1 radiation (1.54060 Å) in a line focus configuration. Linear Williamsom-Hall plots were generated from the line-broadening analysis of the corresponding diffraction patterns [39]. Diffraction patterns were acquired in a Bragg-Brentano geometry with divergent optics (FDS 1/8 and 5 mm mask), a Ni-kβ filter and a 1-D detector. The following ICDD diffraction cards were used as reference: 01–084–5996 for WC, 00–035–0776 for α-W_2C and 00–020–1316 for cubic WC_{1-x}. A zero microstrain reference sample, with average grains size of 30 μm, was prepared by pressurless sintering the WC_{ox} nanopowders at 2150 °C for 2 h inside an Astro® vacuum graphitic furnace.

2.3. Micropillars preparation and testing

Micropillars and lamellae were produced on the polished surfaces within a FIB-SEM dual-column microscope (Helios NanoLab 600i) operated at 30 kV. The pillars were produced following a 2-step approach with two concentric rings milling pattern: initially, a high FIB current (9.3 nA) was used to create a circular trench with the pillar at the centre and, subsequently, at lower current (0.23 nA), the pillar's tapering angle was reduced (Fig. S1 Supp.mat. (a, b)). On average, pillars with 3 μm diameter and 6 μm height were produced in a cylindrical trench with 20 μm diameter. Room temperature compression tests were carried out on the produced micropillars using a Hysitron triboindenter TI950 equipped with a 15 μm-diameter flat punch diamond indenter (Fig. S1 Supp.mat. (e)). Micropillars were compressed under displacement control at rates of 6 nm/s (corresponding to a constant strain rate of $\approx 10^{-3}\, s^{-1}$). To assess the maximum strain, the majority of the pillars underwent compression until failure, while a few tests were stopped at various strain levels to detect any sign of post-compression plastic deformation. The number of pillars tested per sample (Fig. 1, (a)) ranged from 5 to 15, depending on the extent to which structural integrity was maintained at different strain levels. High-temperature compression tests were performed to elucidate any difference in the activation of high-temperature deformation mechanisms between FS and SPS samples. High-temperature tests were carried out in-situ inside a Zeiss SEM Evo using a Hysitron PI88 picoindeter (Fig. S1 Supp.mat. (c)). Micropillars (with a composition corresponding to FS_{pure} and SPS_{pure}) were compressed using a 10 μm-diameter flat punch (Fig. S1 Supp.mat. (d,e)) at strain rates of $10^{-3}\, s^{-1}$ and different levels of strain at room temperature and 700 °C. The contribution of the machine compliance to the obtained load-displacement curves was corrected by comparing the elastic response of the pillars compressed at room temperature with both systems (ex-situ and in-situ).

2.4. Lamellae preparation, TEM and TKD analyses

Electron transparent lamellae were prepared within the FIB-SEM from the pillars previously compressed above their elastic limit, i.e. with maximum strain in excess of 0.2%. The deformed grains contained in the lamellae were observed with a FEI Talos F200x TEM microscope operated at 200 kV. The results were compared with the grains' crystalline orientation and phase composition as acquired by Transmission Kikuchi Diffraction (TKD). TKD analyses were performed by positioning the lamella at a working distance of 5 mm between the electron beam of the FEG-SEM and the EBSD detector, with a tilting angle of 25° with

respect to the horizontal axis. The Kikuchi pattern was acquired at 30 kV with 25 nm step size and processed by AZtecCrystal® proprietary software. For the Kernel Average Misorientation (KAM) calculations, a maximum misorientation angle of 5° (upper threshold misorientation) was selected.

3. Results & discussion

3.1. Microstructure and phase composition

The microstructure and phase composition of the samples as detected by EBSD are shown in Fig. 1(a). As previously pointed out, sintering of the low-oxygen content WC powder produced two materials free from the W_2C phase, but with 6–8 vol% metastable WC_{1-x} phase in the flash product (FS_{pure}). On the other hand, both samples obtained by sintering the oxidised nanopowder are characterised by a biphasic WC/W_2C microstructure (see Fig. 1(a)). The SPS_{ox} sample contains a lower amount of W_2C sub-carbide, around 4 vol%, and possesses finer grain size (Table 1) with respect to the FS_{ox} one. It is interesting to observe that the grain size is around 0.5 μm in the case of SPS, despite the material remaining at the high sintering temperature (2100 °C) for 5 min. Conversely, the flash process, which only lasts 10 s, leads to a more prounced increase in grain size, surpassing 3 μm in the presence of the sub-carbide phase. Abnormal grains, elongated and with a high aspect ratio, are observable in the two samples containing W_2C. SPS_{ox} sample contains only a few abnormal WC grains randomly distributed amongst finer WC and W_2C equiaxed grains, while the FS_{ox} is fully composed of such abnormal grains (Table 1).

The grain boundary migration rate in flash sintered grains can be influenced by lattice defects, particularly those present in the W_2C phase, which is a carbon deficient WC phase known to accommodate larger density of defects [40]. Lantsev et al. proposed a connection between the W_2C phase, abnormal grain growth (AGG) and accelerated diffusion kinetics [17]. Their experimental findings show a lower sintering activation energy in binderless tungsten carbide (BTC) materials exhibiting abnormal grain growth (AGG), suggesting a change in the grain boundary (GB) diffusion. Based on the non-equilibrium grain boundary theory, the activation energy for grain boundary diffusion is influenced by the degree of GB non-equilibrium, which is determined by the density of defects within the boundary. When abnormal grain growth occurs and GB migrate rapidly, they can absorb lattice dislocations distributed amongst the grains. This leads to an exponential dependency of the GB diffusion coefficient on the density of lattice dislocations. As a result, GB migrating into highly defective W_2C grains can absorb a greater number of lattice defects, effectively enhancing their diffusion rate. The strong dependence of GB mobility on the defects density can explain the AGG observed in Fig. 1(a) in the presence of the W_2C phase. The same argument can also be used to explain the superior grain growth in FS_{ox} with respect to FS_{pure} since they are both produced by flash sintering, but no W_2C phase is present in the latter sample. Another possible explanation for the exaggerated grain growth occurring during flash sintering can reside in the actual temperature developed in the material during the flash event, which, if largely superior to that occurring in SPS (2100 °C), can partially explain the boost in diffusion and also in grain growth kinetic. Unfortunately, the temperature during flash is almost impossible to be measured precisely; the black body model by Raj [41], for a theoretical evaluation of the flash temperature, requires the sample to be inserted in a furnace of a known temperature. Nevertheless, if one considers the temperature issue, the large difference in grain growth between FS_{ox} and SPS_{ox} should also be observable between FS_{pure} and its SPS_{pure} counterpart, whose difference is only about 0.5 μm (Table 1). It is also necessary to remember that SPS operates under high uniaxial pressure of 60 MPa, which is well known to contrast grain growth in favour of densifying phenomena [42]. This contribution is absent in the flash process, which operates at negligible uniaxial pressure (4 MPa). In conclusion, the only effect of an extraordinarily high temperature during flash can not justify the excessive grain growth observed in FS_{ox}; therefore, the presence of W_2C phase, in combination with the larger number of defects generated by flash (Fig. 1(b)), must have a role in the occurrence of such phenomenon.

Table 1
Grain size (D_{avg}), aspect ratio of the grains and W_2C content (± standard deviation) of the samples in Fig. 1.

	1) FS_{ox}	2) SPS_{ox}	3) FS_{pure}	4) SPS_{pure}
D_{avg} [μm]	3.17 (±0.55)	0.65 (±0.05)	1.07 (±0.08)	0.53 (±0.06)
Aspect ratio[§]	4.7 (±1.1)	1.7 (±0.6)	1.7 (±0.5)	1.6 (±0.4)
W_2C vol%	38 (±1)	32 (±1)	8 (±1) - WC_{1-x}	/

[§] Defined as the longest axis divided by the shortest axis of carbide grains.

Fig. 1(b) compares the lattice defects (microstrain) of the samples obtained by flash sintering and SPS. The estimate of the lattice microstrain is obtained from the analyses of the line broadening (B_{struct}) of the XRD peaks as a function of sin(θ). The lattice strain can be estimated by plotting $B_{struct}\cos(\theta)$ as a function of $\sin(\theta)$ according to the following equation [39]:

$$B_{struct}\cos\theta = 1.1\frac{\lambda}{crystallite\ size} + lattice\ strain\ (4\sin\theta) \quad (1)$$

The larger the defect concentration in the lattice, the higher the slope of the fitting lines in the two plots of Fig. 1(b). This is the conventional procedure to indirectly estimate the number of defects present in the grains of a sintered material, although the nature of the defects (i.e. 1D-vacancies or 2D-dislocations), cannot be differentiated. As previously stated, the W_2C phase, which is present in SPS and FS materials, is characterised by a larger amount of lattice defects with respect to the WC phase. In all cases, larger microstrain, corresponding to a local distortion of the crystalline order, is measured for FS samples with respect to the SPS ones, being also much higher than the reference sample. The defects density in the FS_{ox} sample is almost double with respect to the SPS_{ox} one, thus agreeing with the explanation given before for the AGG observed in Fig. 1(a), which represents further proof of the higher number of defects introduced by the flash process.

3.2. Room temperature pillars' deformability

Fig. S2 (Supp.mat.) shows some FESEM images of the pillars where the different microstructures of Fig. 1(a) are easily recognised. After the FIB milling, the pillars taper angle is reduced to ≈ 3.5° (Fig. S2 Supp. mat.), allowing a precise evaluation of engineering stress and strain as:

$$\sigma_{eng} = \frac{F}{A_0} \quad (2)$$

$$\varepsilon_{eng} = \frac{\Delta L}{L_0} \quad (3)$$

from the recorded data of force (F) and displacement (ΔL), A_0 and L_0 being the initial micropillar average diameter and height, respectively. The specific selection of pillar's dimensions allowed to prepare microsamples from both SPS and FS materials almost free of pores (Fig. S2 Supp.mat.). It is important to point out that flash sintered materials exhibit a larger residual porosity, approximately in the range of 3–5%, whereas in the case of SPS materials, the residual porosity is typically less than 1%.; such difference can be significant when mechanical properties are compared at a larger scale [43]. At the micron scale, a single pillar contains, according to the microstructure of Fig. 1, from tens to hundreds of individual grains (Fig. S2 Supp.mat.). This allowed to study the deformability of polycrystalline monolithic tungsten carbide, instead of single crystals, at a size scale small enough to delay the unstable crack propagation and up to stress levels comparable to those required to activate plastic deformation mechanisms.

Figs. 2 and 3 show the stress-strain curves and post-compression

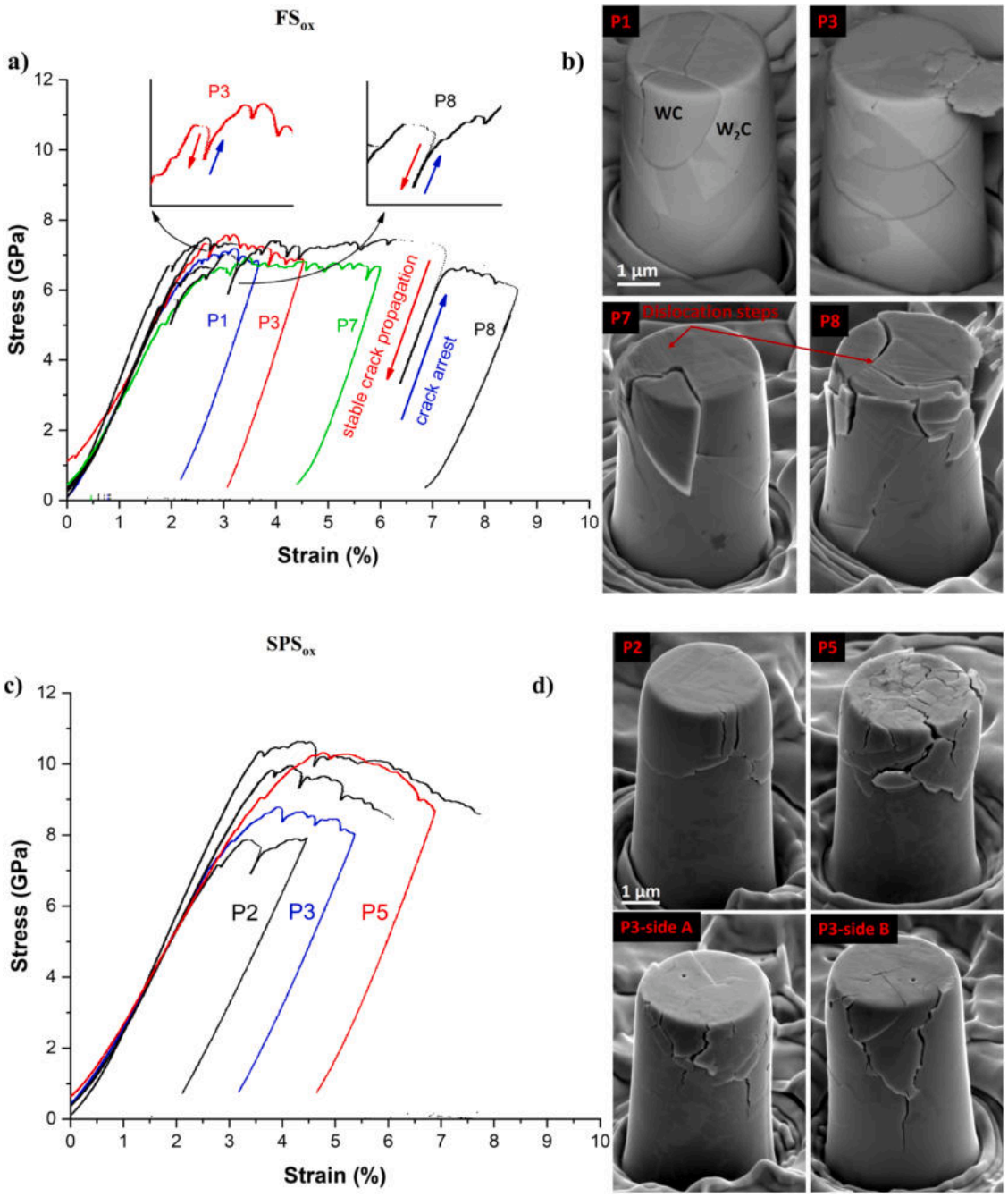

Fig. 2. Stress-strain curves obtained from room-temperature compression of FS_{ox} (a) and SPS_{ox} pillars (c) and corresponding FESEM images (b, d) of plastically deformed pillars at different strain levels before final failure. The insets in FS_{ox} (a) show magnified views of crack arrest events. Tested pillars are identified as 'P1', 'P2'… to correlate the stress-strain curves with the corresponding FESEM micrographs.

FESEM images of pillars compressed above their elastic limit but before their catastrophic failure. As previously mentioned, the micrometric pillar dimension allows to reach stresses as high as 10–11 GPa, in a condition of stable crack propagation, which is a testament to the strong bonding of the sintered grains; for comparison, pillars prepared from WC single crystals have an ultimate strength in the range of 2–5 GPa (prismatic orientation) and 20–25 GPa (basal orientation) [44]. In almost all the curves of Figs. 2 and 3, the pillars did not fail in the elastic regime, and different deformation mechanisms were activated before the final failure accounting for a certain degree of permanent deformation.

3.2.1. Room temperature deformability of SPS pillars

Pillars extracted from SPS samples possess the highest yield stress: 10 GPa for SPS_{ox} and around 11 GPa for SPS_{pure}. The two materials show an elastic behaviour up to higher stress levels when compared to FS pillars. In addition, SPS pillars behave differently after reaching the yield point since they show a partial strain hardening behaviour up to the ultimate strength and a decrease in the stress for increasing strain (strain-softening) up to the failure. In traditional tensile tests, the region of neck formation is where the reduction of the resistive cross-sectional area occurs, this region being where the apparent strain-softening behaviour is observed in the engineering stress-strain curve. SPS_{ox} and, partially, SPS_{pure} show both strain-hardening and strain-softening regions. It is possible to explain the strain-softening behaviour shown in most SPS_{ox} curves with the same argument used for neck formation in a macroscopic tensile test i.e. with a reduction in the material's resistant

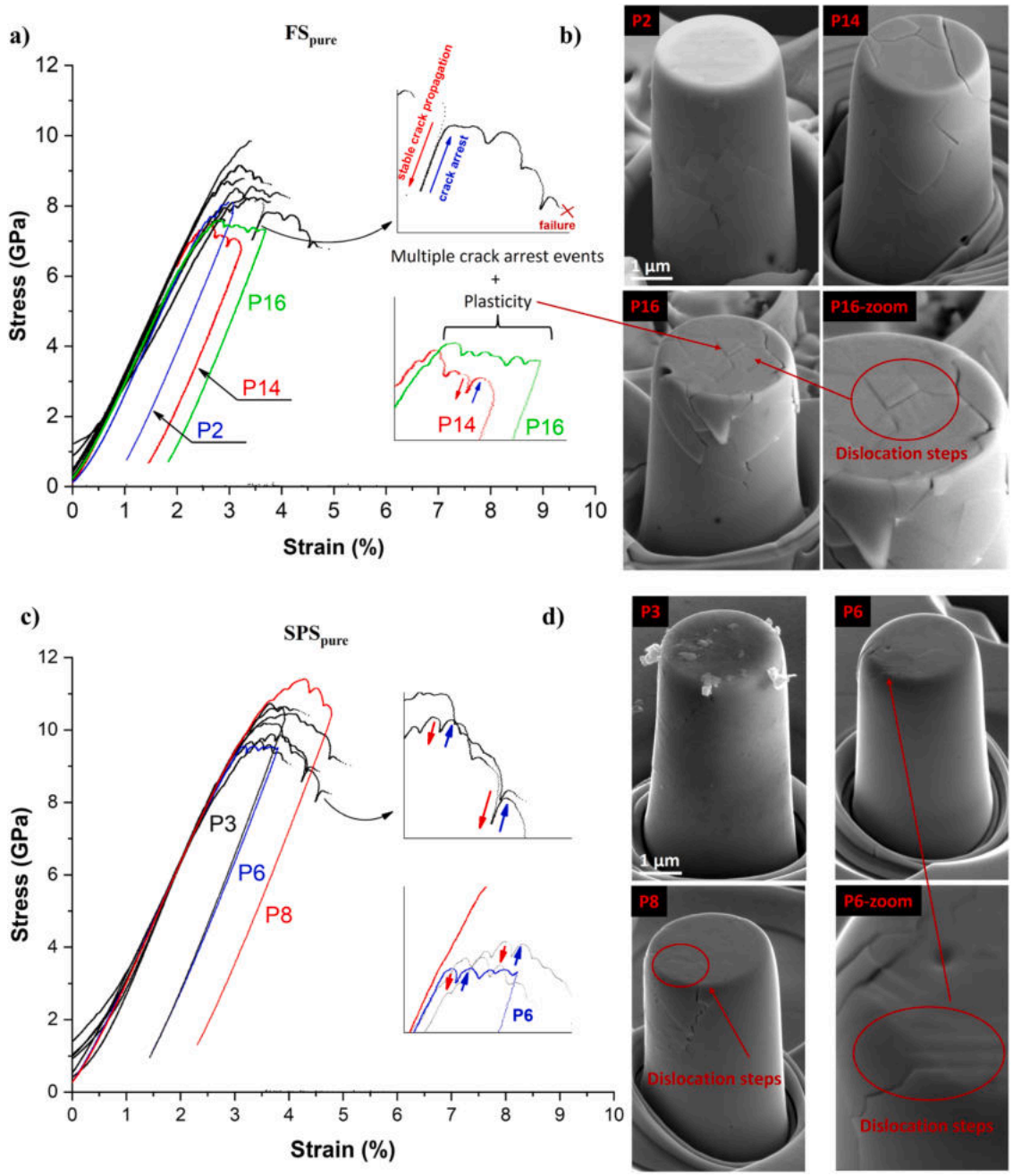

Fig. 3. Stress-strain curves obtained from room temperature compression of FS_{pure} (a) and SPS_{pure} pillars (c) and corresponding FESEM images (b, d) of pillars, plastically deformed at different strain levels. The insets show magnified views of crack arrest events. Tested pillars are identified as 'P1', 'P2'… to correlate the stress-strain curves with the corresponding FESEM micrographs.

cross-sectional area. Post-compression SPS_{ox} pillars (Fig. 2(d)) show an extensive microcracking which influences the resistant area i.e. the portion of material supporting the load. As a matter of fact, compressed pillars in Fig. 2(d) show a remarkable increase in the observable microcracking with permanent strain from P2 to P5, this being associated with an extension of the strain-softening regions (Fig. 2(c)). It is worth noting that SPS biphasic microstructure (WC/W_2C) tolerates a much higher permanent strain with respect to the monophasic SPS_{pure} counterpart (Fig. 3(c)), at the expense of a lower maximum strength and a lower stiffness. The W_2C phase is generally considered brittle and detrimental in WC products, responsible for lower macroscopic hardness and toughness [45]. However, in the presence of the W_2C phase in the WC/W_2C composite, the SPS_{ox} pillars reached the highest strain (up to 7%), with a considerable portion of permanent deformation.

Plastic deformation occurs simultaneously with crack propagation and is accompanied by stress drops/strain jumps. Jones et al. [44], in their micropillar compression study of WC single crystals, suggested that these instantaneous load drops can be caused by intermittent plastic slip and/or by crack propagation. Evidence of plastic deformation during the room temperature compression of the two SPS pillars is limited to the presence of some dislocation steps on the top surface of pillars compressed at the highest strains (see P6 and P8 in Fig. 3(d).

With the aim to disclose the connection between these instantaneous load drops (red and blue arrows in the insets of Fig. 3 (a, c)) with the activation of plasticity, the cross-section of deformed pillar P6 was analysed by TEM (Fig. 4). After the compression test, a lamella was prepared by FIB milling from the deformed SPS_{pure} pillar P6. Such pillar was deformed plastically to about 1% strain, as shown from the

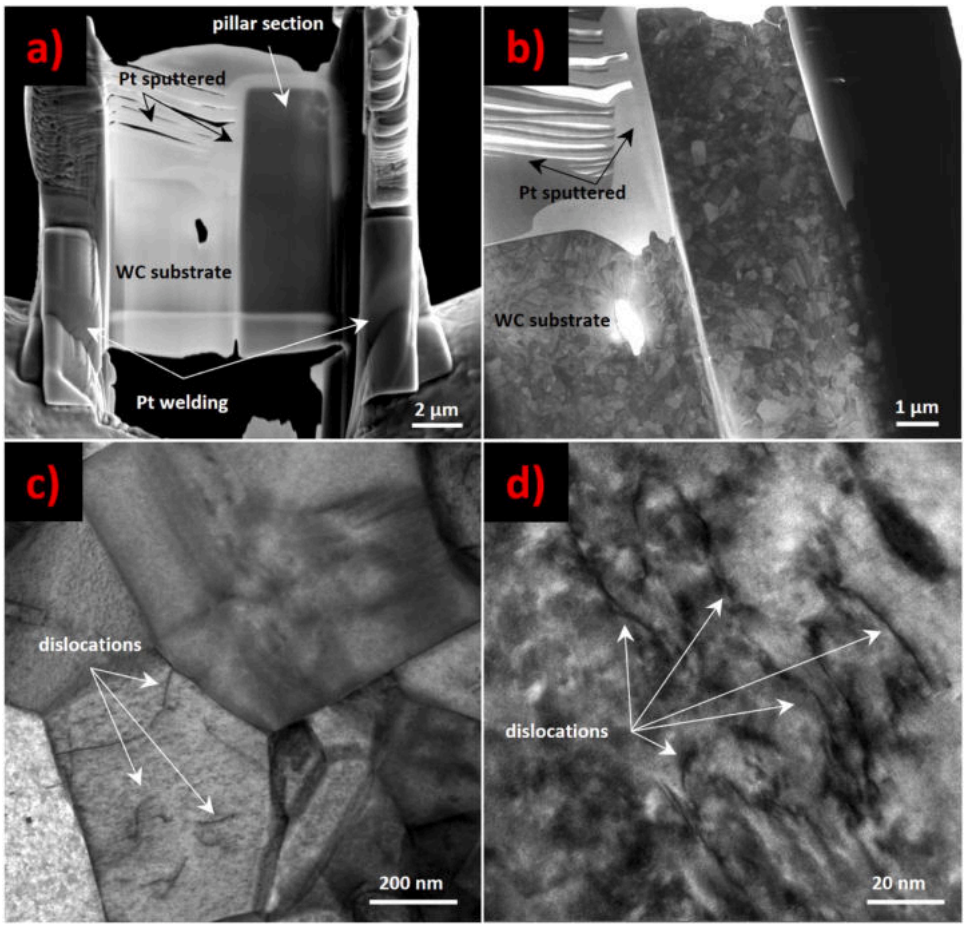

Fig. 4. Electron transparent lamella containing a cross-section of the SPS pure P6 pillar. FESEM image of the lamella during its preparation inside the FIB-SEM microscope (a) and its low magnification TEM image (b). HRTEM images of some grains contained in the lamella (c) and (d). White arrows highlight the presence of undissociated dislocations.

unloading curve in Fig. 3(a). Fig. 4 (c, d) shows the presence of undissociated dislocations in the deformed grains of pillar P6, which, once reaching the surface, generate the dislocation steps shown in Fig. 3(d). Plasticity, intended as dislocation motion, has a role in the occurrence of such intermittent load drops, and it is very probably competing simultaneously with crack propagation and arrest. The inset in Fig. 3(c) shows several sharp stress drops and jumps during the compression of the P6 pillar, these events being very likely correlated with the crack initiation (sharp drop of the stress) and subsequent arrest (stress surge). This phenomenon occurs several times before the catastrophic failure of the pillar or its unloading. During these multiple crack propagation and arrest events, the material experiences (i) stable crack propagation along multiple paths (microcracking) and (ii) the presence of a minor dislocation activity (Fig. 4 (b, d)). This multiple crack arrest mechanism is evident in almost all compression curves (Figs. 2 and 3), for both SPS and FS pillars. This is why most of the pillars do not fail in a brittle manner but can be compressed plastically in a condition of stable crack propagation.

In summary, polycrystalline tungsten carbide possesses, at the micro-scale, a toughening mechanism associated with micro-cracking at limited strain levels. Since this mechanism is present in all samples but is activated at different stress levels, it can be used to understand the different deformability of WC products at room temperature. This toughening mechanism is much more active in SPS_{ox} pillars than in SPS_{pure} ones, which is associated with the ability of SPS_{ox} pillars to resist more intense crack extension and, thereby, to reach much higher strain levels before failure. The only difference between the two SPS materials is the presence of the W_2C phase, which must certainly play a role in increasing the efficiency of this toughening mechanism.

3.2.2. *Room temperature deformability of flash-sintered pillars*

The presence of the W_2C phase contributes to reach a larger maximum strain also in flash-sintered FS_{ox} pillars (Fig. 2(a)) with respect to FS_{pure} ones (Fig. 3(a)). For example, P8 sample (Fig. 2(a)) reaches very high strains (about 9%) without failure. Nevertheless, unlike SPS_{ox} and SPS_{pure} specimens, FS_{ox} pillars deform plastically without significant stress drop; in other words, after the elastic region, the curve remains flat without the strain-softening effect observed for SPS pillars. This flat region, corresponding to FS_{ox} pillars undergoing plastic deformation, is again characterised by crack propagation and arrest events. Like in the SPS_{ox} counterpart, the nature of these intermittent load drop events is connected with extensive pillar cracking. The compression of FS_{ox} pillars at increasingly higher strain levels (corresponding to 3, 4, 6 and 9% from P1 to P8 (Fig. 2(b)), is accompanied by further crack propagation. However, before being unloaded, such extensively damaged pillars can still sustain stresses of about 6–7 GPa, denoting peculiar high damage tolerance and toughness. This high toughness is associated with the tendency of microcracks to propagate along multiple paths during the irreversible deformation of FS_{ox} pillars and with a dislocation-mediated plastic deformation, as observed in P7 and P8 in Fig. 2(b).

The grain size in FS_{ox} is much larger than in SPS_{ox}.This relates to the larger maximum strain and the different shape of the stress-strain curve which is flat after the material's yield point without noticeable strain hardening and softening behaviour. This is connected to the strong dependence of plasticity on WC grain size [46], which, in turn, is

associated with the active slip systems in WC crystals at room temperature. Recently, in-situ compression studies of single crystal WC pillars [44], lattice rotation axis analyses [47], and slip traces coupled with EBSD and HRTEM analyses [46] have found enough evidence to unravel the complexity of the highly anisotropic plasticity of WC grains. At room temperature, the prismatic slip systems $\{10\bar{1}0\}$ are favoured: $[11\bar{2}0](\bar{1}100)$ and $[1\bar{2}10](\bar{1}010)$; while the basal one, $[0001](01\bar{1}0)$, is considered a secondary slip system. For this reason, grains favourably orientated for prismatic slip deform more easily than those favourably orientated for basal slip. Nabarro et al. predicted, by first-principles density functional theory simulations, that the Peierls stress for the basal dislocations $[0001](01\bar{1}0)$ are twice that for prismatic dislocations

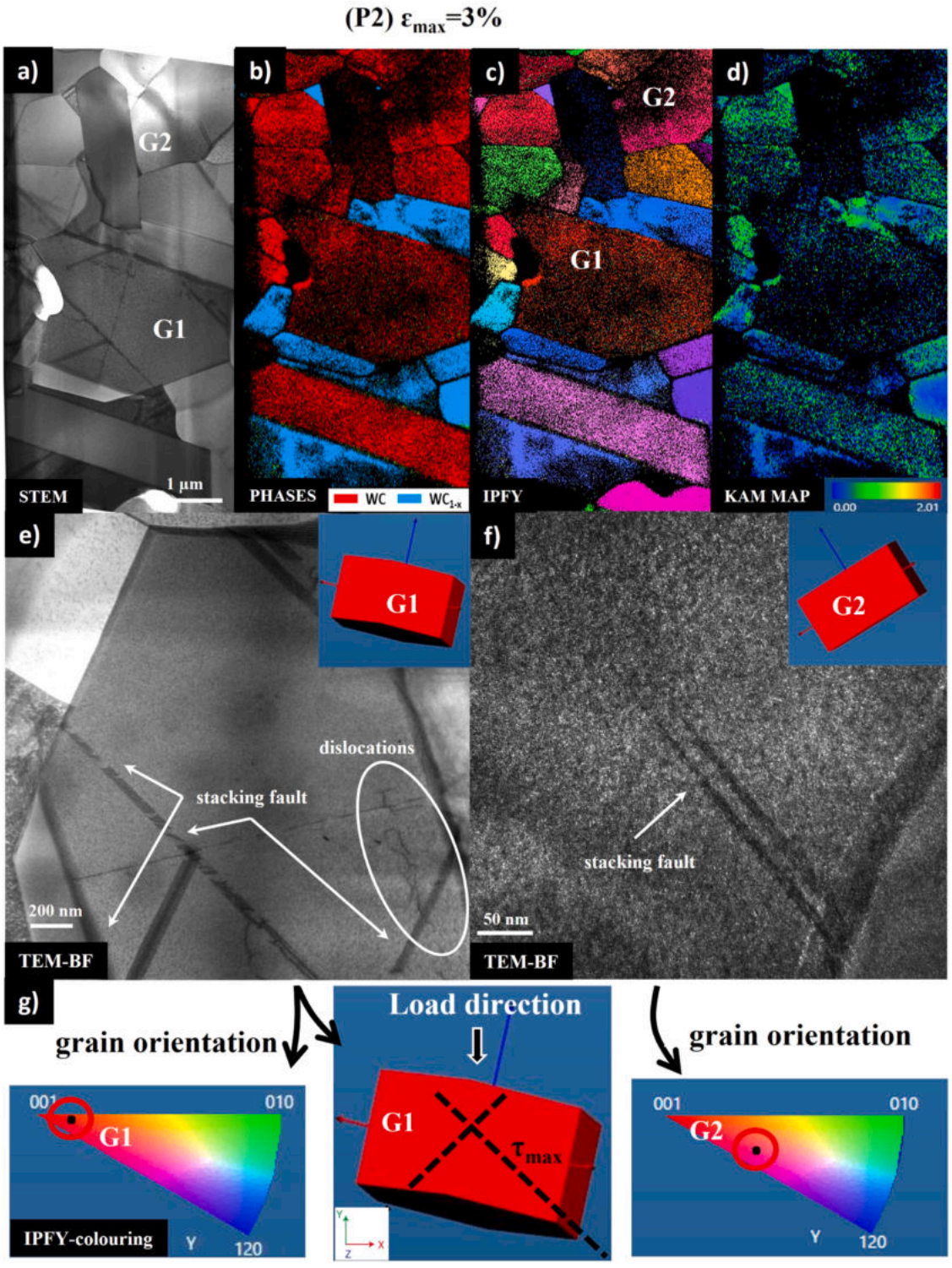

Fig. 5. HRTEM and Transmission Kikuchi Diffraction (TKD) analyses of a lamella containing the cross-section of FS_{pure} P2 pillar after compression. STEM view of the deformed grains contained in the sectioned pillar (a), together with its phase composition (b), orientation analysis (c) and measure of the local strain gradient: Kernel Average Misorientation (KAM) map (d). Bright field (BF) TEM micrographs of grain G1 (e) and G2 (f) containing stacking faults; the insets represent the grains orientation. Orientation relationship between the IPF-Y map, the load and the maximum resolved shear stress directions (g).

on $\{10\bar{1}0\}$ [48,49]. The high anisotropy between prismatic and basal-orientated grains also reflects the huge difference in their nano-indentation hardnesses: 29 GPa (prismatic) against 53 GPa (basal) [50]. This anisotropy was also detected in the transition from a stochastic to deterministic flow stress in basal-orientated WC single-crystal pillars. This transition was observed between pillars with 1 μm and 5 μm in diameter: the former shows a stochastic flow stress, related to the probability of having an already present dislocation in the crystal, while in the latter, all crystals deform in the same way, because the larger pillar/crystal size allows dislocations to pile-up so that the stress levels required to both nucleate and propagate a dislocation are reached [44]. Therefore, the different plastic behaviour of SPS_{ox} and FS_{ox} pillars, which possess the same biphasic WC/W_2C composition, can be mainly related to the exaggerated grain size generated by the flash sintering process: much larger WC crystals in FS_{ox} (3–5 μm with respect to 0.5 μm in SPS_{ox}) can favour the activation of both prismatic and basal slip systems. This increased plasticity is then reflected in the higher ability of the damaged material to resist catastrophic failure because of the more intense activation of the intrinsic toughening mechanism (Fig. 2 (a,b)).

FS_{pure} pillars (Fig. 3(a,b)) show an intermediate maximum stress

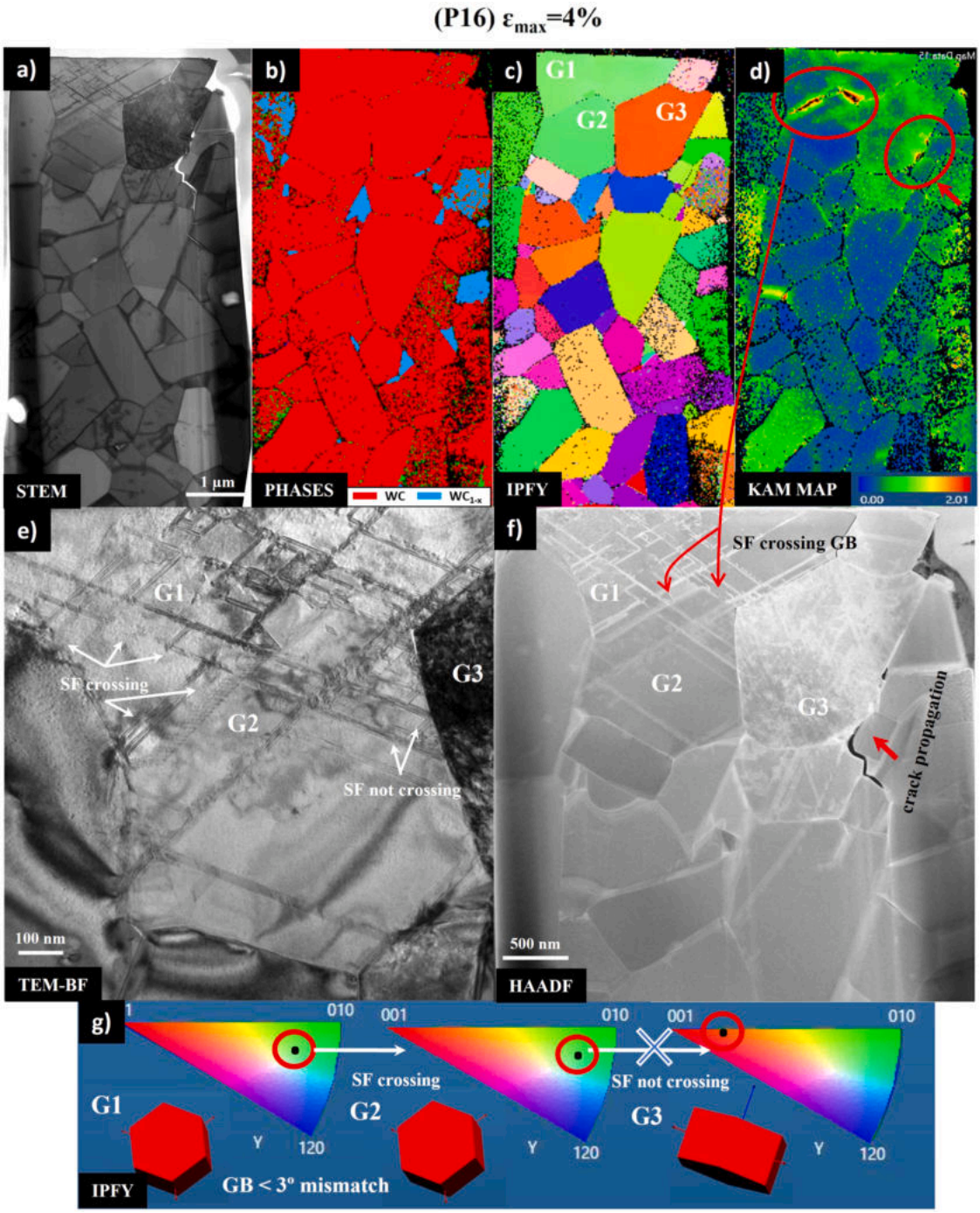

Fig. 6. HRTEM and TKD analyses of a lamella containing the cross-section of FS_{pure} P16 pillar after compression. STEM view of the deformed grains contained in the sectioned pillar (a), together with its phase composition (b), orientation analysis (c) and measure of the local strain gradient by KAM map (d). Bright field (BF) (e) and High-angle annular dark-field (HAADF) (f) TEM micrographs of a highly deformed pillar region containing G1, G2 and G3 grains. IPFY colouring map and orientation (g) relationship between G1, G2 and G3 grains, pointing out the mismatch conditions for dislocation to cross the GB between two hexagonal WC grains.

with respect to FS_{ox} and SPS_{pure} ones. They are also stiffer and stronger than FS_{ox} specimens, although the maximum strain is lower. It is difficult to disclose if this reduced maximum strain is due to the absence of W_2C phase or the finer grain size (Table 1). FS_{pure} pillars have inferior mechanical properties with respect to SPS_{pure} ones, in terms of yield/ultimate strength and deformability (Fig. 3). They also show the largest variability amongst all the materials tested, some pillars reaching a yield strength of about 7 GPa, and others being loaded elastically up to 8–9 GPa. The compression curves of FS_{pure} pillars show the previously discussed intermittent load drops, together with dislocation steps (like P16 in Fig. 3(b)). The majority of FS_{ox} pillars failed catastrophically at unpredictable strain levels and this required to test a much larger number of pillars (up to 16) to be able to save three pillars loaded at increasing strain levels (P2, P14 and P16 in Fig. 3(b)). This high variability in the probability of failure can be caused by strong competition between the strain energy dissipation mechanisms, namely crack propagation and dislocations motion. Hence, to better understand when the deformation mechanism is activated with respect to grains orientation and initiation/propagation of the crack, two of the three saved pillars were analysed by TEM and TKD.

Figs. 5 and 6 summarise the analyses of the grains composing two FS_{pure} pillars (P2 and P16 in Fig. 3(a,b)) deformed at maximum strains of 3% and 4%, respectively. In both pillars, the majority of the dislocations involved in the plastic deformation are partial dislocations hence, several stacking faults (SF) can be observed in the deformed grains. It is possible to conclude that the observed SFs are the result of deformation because: (i) all the SF share the orientation with one of the two directions of maximum shear stress (τ_{max}), as indicated in Fig. 5(g), and (ii) partial dislocations cross a grain boundary between G1 and G2 grains, forming a continuous SF amongst the two grains, as represented in Fig. 6(e, g). Liu et al. reported that partial dislocations contribute significantly to the plastic deformation and toughness of WC crystals [46].

In P2 specimen (Fig. 5), only few grains contain a trace of the movement of partials, i.e. stacking faults. For example, Fig. 5(e,f) shows the presence of some SF in two hex-WC grains, denoted as G1 and G2. The low KAM (Kernel Average Misorientation) map intensity confirms such limited dislocations concentration (Fig. 5(d)). KAM is a measure of the local distortion in the orientation of a crystal, and it is directly related to the dislocation density in a crystalline material. The area of high magnitude in the KAM map corresponds to strain concentration, i.e. more deformed material [46]. Comparing the two KAM maps of Figs. 5 and 6, which possess the same colour gradient, it is easy to conclude that the grains in P2 sample experienced very modest plasticity. On the other side, grains in P16 specimen, especially those near the top of the pillars, are completely full of SF and, indeed, the KAM map of Fig. 6(d) has a stronger magnitude in correspondence with such grains. The dislocation activity amongst the two samples differs significantly, while the total deformation of the two pillars, P2 and P16, differ only by 1%. The compression curve for P16 in Fig. 3(a,b) reaches 4% strain before the pillar is unloaded. We believe that the sample was very close to failing at this strain since the majority of FS_{pure} pillars (Fig. 3(a, b)) broke at a very similar, if not lower, strain. Also the KAM map in Fig. 6(d) suggests that the strain concentration reached at the grain boundary between grains G1 and G2 is very close to the strain level achieved near the regions of crack propagation. A polycrystalline material requires that slip propagates from one grain to the other to plastically deform in a condition of "easy glide" (absence of strain hardening). Fig. 6 shows that this is possible amongst two h-WC grains only when their orientation does not differ significantly. In Fig. 6(g), partials can cross the GB between G1 and G2 because the orientation difference is lower than 3°, but they cannot cross into G3 since the mismatch is much larger.

The stress required for a dislocation to cross the GB, in the almost perfect condition of two well-orientated grains, is close to the stress required for a crack to propagate. This can be deduced from the large difference in concentration of SFs between the surface and the middle and bottom parts of the P16 pillar (Fig. 6(a)). SF activity ends by reaching the bottom region of G3 in (Fig. 6(f,d)) where the big crack present competes in releasing the strain energy accumulated during the compression of the pillar (Fig. 6(f)). The analyses reported in Fig. 6 represent a good example of why an arbitrary deformation is so difficult in these polycrystalline pillars and why they fail stochastically at different strain levels (Fig. 3(a,b)). The amount of strain energy required for activating plasticity in the WC grains competes with the mechanisms of energy release operated by the generation of new surfaces by crack advancement. Plasticity in WC crystals is anisotropic and according to the literature previously reported, i.e. on the slip systems active at room temperature, it is favoured in such grains orientated with the prismatic faces in the direction of the applied load and disfavoured for those with a basal orientation. Fig. 7 summarises the different preferential grains orientation for the two pillars analysed in Figs. 5 and 6, and shows how the low dislocation activity in P2 sample of Fig. 5 can be imputed to the disfavoured orientation of the grains contained in such pillars, which are almost completely basal orientated. The basal orientation corresponds to the red colour of the majority of grains in the IPFY map of Fig. 5(c), while the highly deformed grains contained in the top portion of P16 of Fig. 6(c) show colours towards the green, that corresponds to a prismatic orientation.

In conclusion, the room-temperature deformability does not differ significantly between the materials consolidated by flash sintering and spark plasma sintering, in the presence and absence of the W_2C phase, hence between FS/SPS_{pure} and FS/SPS_{ox} samples.

3.3. High-temperature pillars deformability

At room temperature, tungsten carbide possesses a limited number of independent active slip systems (lower than 5), making the material extremely hard and brittle. At room temperature, the plastic strain is limited, and the stress-strain curves have a stochastic nature, depending on the orientation of the grains in the pillars and on pre-existing defects. By increasing the temperature, new slip systems become available in WC crystals allowing more intense plastic deformation. A third prismatic slip system $[\bar{1}\bar{1}23](\bar{1}100)$ and the basal one $\{0001\}$ become available at around 600 °C [44]. An additional candidate can be $[11\bar{2}0](0001)$ via a cross-slip mechanism of $\langle a \rangle$ dislocations from prismatic to basal planes [44]. The increased plasticity in the range 600–700 °C is also reflected in a two to three-fold drop in the hardness of carbide grains [50,51].

The effect of temperature on the increased deformability of polycrystalline tungsten carbide tested in-situ by the Hysitron PI88 picoindeter (Fig. S1 Supp.mat. (c)) is reported in Fig. 8. Pillars produced from FS_{pure} and SPS_{pure} materials were tested at RT and 700 °C. The RT compression curves are very similar to those reported in Fig. 3. SPS_{pure} and FS_{pure} pillars are extremely stiff at room temperature, reaching a maximum strength of about 8 GPa (FS_{pure}) and 9.5 GPa (SPS_{pure}) in the elastic regime, with very limited plastic deformation. The catastrophic

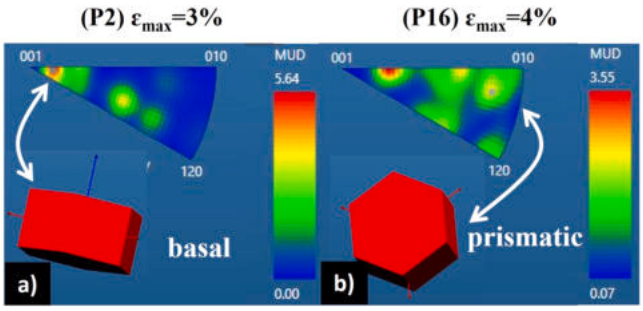

Fig. 7. IPFY maps coloured according to the MUD scale; MUD>1 represents a preferential orientation of the grains in the lamella. The two maps report the preferential orientation of P2 (a) and P16 (b) pillars of the FS_{pure} series.

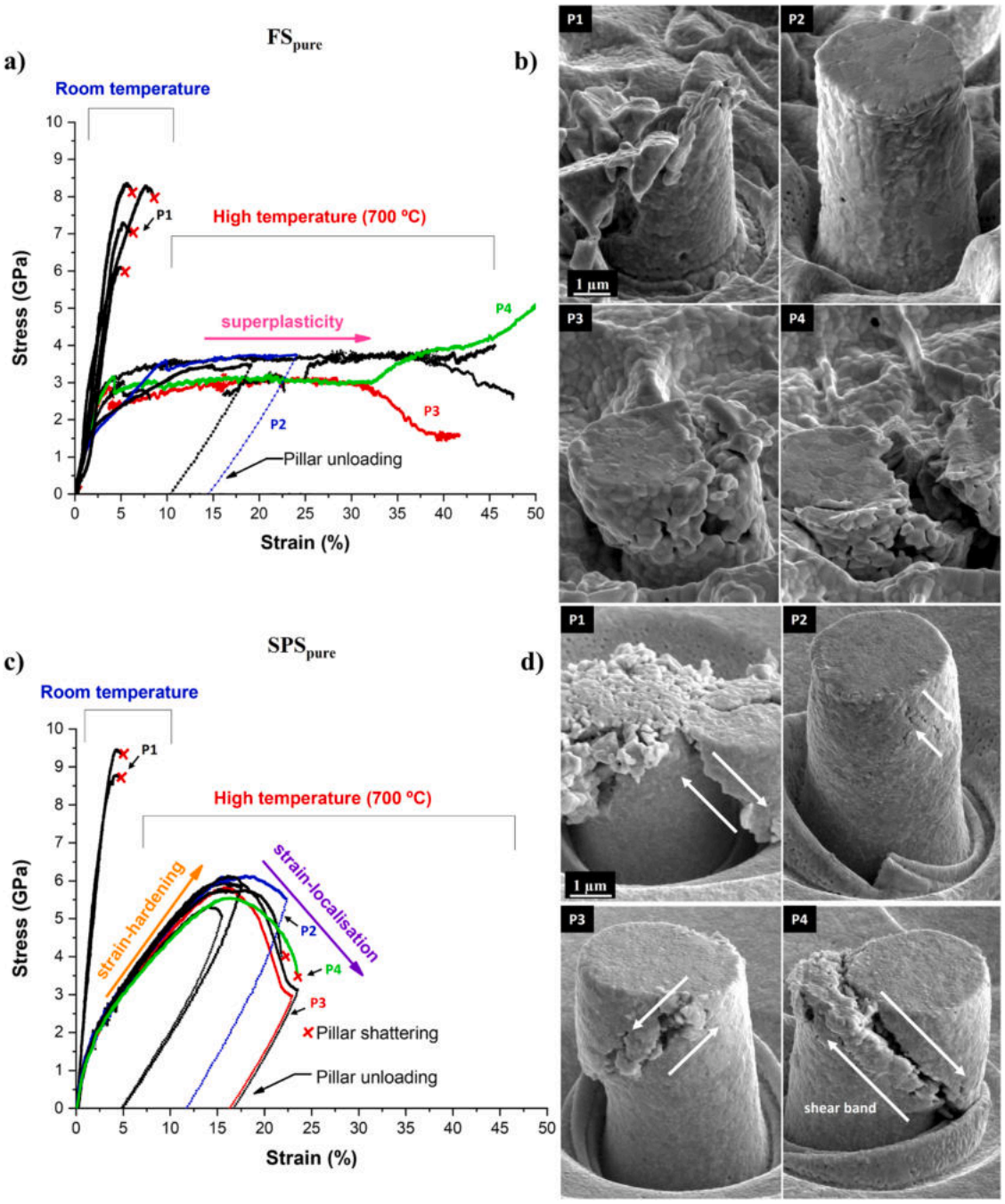

Fig. 8. Stress-strain curves obtained from in-situ compression test at room and at high temperature (700 °C) of FS_{pure} and SPS_{pure} pillars (a, c) and corresponding FESEM images (b, d) of pillars, plastically deformed at different strain levels The curves where the load drops instantaneously to zero are indicated with a red cross and refer to the shattering of the pillar.

failure event is almost instantaneous and ends with the complete shattering of the pillar.

At high temperature (700 °C), stress-strain curves shown in Fig. 8 reveal a significant increase in the deformability of the material along with a substantial reduction in the pillars' strength. SPS_{pure} pillars, characterised by a tensile strength of 8–9 GPa at RT, are plastically deformed at a yield of around 1.5–2 GPa at 700 °C. Similar behaviour is shown by FS_{pure} pillars up to the onset of plasticity. This behaviour can be indeed correlated to the activation of new slip systems in WC crystals in the temperature range 600–700 °C, at which considerable differences in the deformation behaviour between FS and SPS pillars can be observed. SPS_{pure} pillars deform plastically with a strain-hardening behaviour up to their maximum strength (Fig. 8(c)), the stress then decreasing at larger strain (strain-softening). Images of deformed P2, P3 and P4 pillars (Fig. 8(d)) clearly show that strain localisation events occur during the strain-softening regime. Shear bands appear at 45° on the surface of the deformed pillars (directions of maximum shear stress), which causes instability in the deformation. This loss of deformation homogeneity leads to catastrophic failure when the resistive cross-section cannot support the high loads. Fig. 8(b) shows the state of a pillar before (P3) and after (P4) this failure event. The top portion of such pillars slides down at the fracture stress and maximum strain that the pillars can support in correspondence with the shear band. All SPS_{pure} pillars tested at high temperature share the same deformation behaviour and fail catastrophically at a maximum strain of around 25%.

On the other hand, FS_{pure} pillars (Fig. 8(a)) show little strain-

hardening and no strain-softening behaviour. All the tested pillars were deformed at 700 °C in a condition of almost perfect plastic deformation, without or with a very limited strain-hardening. For example, FS_{pure} P2 sample shows the pillars' state during the plastic flow, at a strain level of around 20% where there is no evidence of crack propagation events as observed for the SPS_{pure} P2 pillar. These pillars can be deformed up to an outstanding value of maximum strain of 50% without the occurrence of shear-bands (Fig. 8(b)), hence without the loss of homogeneity of deformation. It is thereby possible to conclude that at 700 °C, the flash-sintered WC material can be plastically compressed up to very high strain levels (50%) without strain localisation events, thus showing a phenomenon known as superplasticity [52].

3.4. Superplasticity in flash-sintered pillars & grain boundary sliding

Superplasticity is a unique mechanical behaviour shown by specific materials which allows them to undergo significant plastic deformation before failure [52]. The remarkable 50% strain exhibited by FS_{pure} pillars under constant stress conditions (Fig. 8(a)) demonstrates an exceptional high-temperature ductility exclusively attributed to the phenomenon of superplasticity. This characteristic is typically associated with ceramics that possess a fine-grained microstructure and is primarily driven by grain boundary sliding. Grain boundary sliding was observed in various fine-grained ceramics such as SiC, Si_3N_4 and yttria-stabilized zirconia [53,54].

A crucial requirement for superplasticity to occur is the presence of accommodation processes that compensate for the cavities and cracks inevitably generated during the sliding of rigid ceramic grains. In some cases, superplasticity is observed in materials like Si_3N_4 when a glassy phase is present at the grain boundaries [55]. Alternatively, accommodation mechanisms can involve diffusion and dislocation motion, enabling the sliding of adjacent grains and maintaining the grain compatibility. The diffusion mechanism facilitates stress redistribution and allows for substantial deformations without fracturing.

A closer look at the grains contained in the FS_{pure} pillars (Fig. 9) reveals how superplasticity is the result of GB sliding. Red arrows in Fig. 9 indicate the areas of the pillars where there is a step height difference between adjacent grains, generated upon their motion from their original positions. Both, SPS_{pure} and FS_{pure} materials are characterised by very similar clean GB, clearly without any sign of glassy phase and with minor Cr impurities (Fig. S3, Supp.mat). However, it is important to point out that only flash sintered pillars (FS_{pure}) can be deformed to around 50% strain without macroscopic failure.

After the large strain experienced by the materials, grains remain equiaxed in the heavily deformed FS_{pure} pillars (Fig. 9). The same equiaxed shape can be observed for the grains present in the undeformed regions around the pillars (Fig. 9) and for the original grains before the thermomechanical compression tests (Figs. 1, 5 and 6). This is consistent with the phenomenon of GB sliding, the grains shape not changing even after 50% of strain, with no sign of elongation in a preferred orientation. The undeformed state of the grains in the pillars of Fig. 9 is another important evidence of how the majority of the deformation achieved for the FS_{pure} pillars was driven by only GB sliding and not by dislocation-motion within the grains. Rodriguez et al. observed that in superplastic MgO specimens [53], there was a lack of dislocation activity and no work hardening in the stress-strain curve, similarly to Fig. 8(a). They also noted the preservation of equiaxed grain microstructure.

It is intriguing to observe that superplasticity occurs exclusively in the flash-sintered material, although SPS_{pure} pillars possess finer grains compared to FS_{pure} ones (Figs. 8(b, d) and 1). Therefore, the discrepancy in high temperature deformability between the two materials can not be attributed solely to distinct microstructural features but must be sought in other characteristics introduced during the flash sintering process. For instance, previous research correlated the increased plasticity observed in YSZ [30] and TiO2 [31] after flash sintering to the introduction of a significant number of defects such as vacancies and/or dislocations. Fig. 1(b) illustrates that the flash sintered material, FS_{pure}, which exhibits superplastic behaviour, is characterised by a higher density of crystalline defects. Notably, the cubic WC_{1-x} phase in the FS_{pure} material possesses remarkably high microstrain. This increased microstrain observed in both h-WC and c-WC phases of FS_{pure} material also found a correlation with the presence of "post-flash" dislocations detected during the TEM observation (Fig. S4, c; Supp.mat.). Undissociated dislocations were found in the regions where the material was not subjected to external stress.

In addition to these findings, it was observed that flash sintering is capable to modify the grain boundaries of sintered oxide ceramics, promoting atomic migration [24,56], redistribution of oxygen vacancies [57,58] and altering grain growth kinetic [59,60]. The significant impact of the structure, nature and chemical bonding of grain boundaries (GB) on the flow stress during superplasticity indicates that a potential alteration of the GB resulting from the flash event may account for the flash sintered pillars' capability to facilitate the rigid sliding of ceramic grains, thus avoiding the occurrence of visible macroscopic shear bands as observed in the SPS samples (Fig. 8(d)). However, for non-oxide ceramics like tungsten carbide (WC), there is currently a lack of sufficient research data that elucidates any potential modifications of grain boundaries triggered by the flash sintering process. This

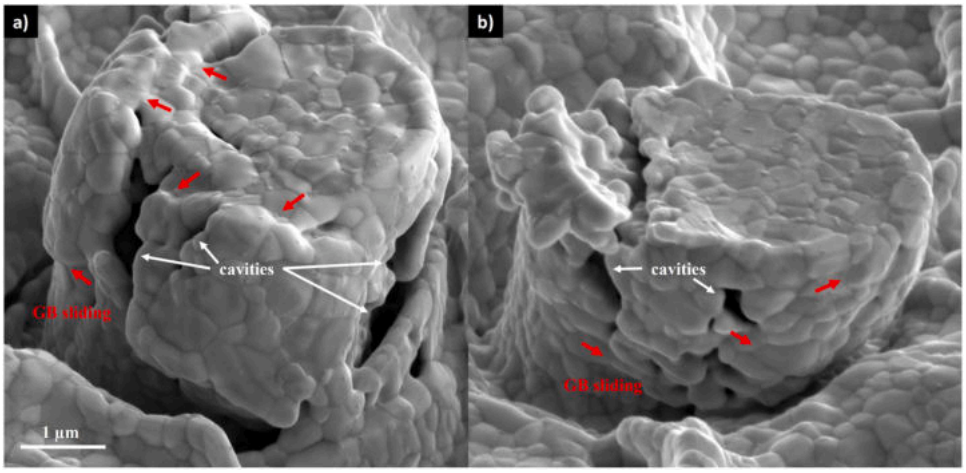

Fig. 9. High magnification FESEM images of two FS_{pure} pillars deformed up to 50% strain at 700 °C. Grains are visible in the two pillars because the material was exposed to 700 °C during in-situ compression in SEM high-vacuum atmosphere. Grain boundary (GB) sliding, as indicated by the red arrows, occurs where there is a step height difference between adjacent grains, while white arrows indicate cavities formation from rigid sliding of ceramic grains.

knowledge gap obscures a possible connection with the mechanism of grain boundary sliding, the post-flash defects and the mobility of atoms at such boundaries. Nonetheless, the fact that the FS_{pure} pillars can deform uniformly without the shear instability and the strain-hardening observed in the SPS pillar of Fig. 8(c, d) suggests the involvement of distinct diffusion-controlled accommodation mechanisms. The flash event might have the capacity to modify the nature of the grain boundaries, enhancing the grains' ability to slide against each other at a lower flow stress, below the threshold required to activate dislocation-mediated plasticity within the grains. Future research efforts should concentrate on investigating the characteristics of grain boundaries in materials consolidated using fast and ultrafast sintering techniques, with the aim of determining whether and how flash sintering can enhance the mobility of atoms across grain boundaries.

4. Conclusions

Polycrystalline binderless tungsten carbide (BTC) micropillars can withstand a certain degree of permanent deformation while maintaining a relatively high load-bearing capability. During room-temperature compression, micropillars prepared from both SPS and FS processes show a toughening mechanism associated with stable crack propagation and arrest events. These toughening effects correspond to intermittent load drops/surges within the stress-strain curves of the compressed pillars and allow them to accommodate some degree of permanent deformation. At room-temperature, this toughening mechanism is not affected by the sintering process, although it is correlated with the presence of the subcarbide (W_2C) phase within the WC matrix.

Conversely, at high temperature (700 °C), FS pillars possess a superplastic behaviour reaching deformations up to 50% without failure. Also the material consolidated by SPS shows increased deformability at 700 °C, although none of the pillars tested in this work survived strains above 25%. The strain is not homogeneous in SPS pillars, causing the material to fail because of a macroscopic slide at shear bands.

Flash sintering is demonstrated to enhance the high-temperature deformability of tungsten carbide. The superplastic behaviour at 700 °C occurs because the flash sintering alters the accommodation mechanism of GB sliding, this allowing the material to deform homogeneously up to very high strain levels. In light of such results, it will be crucial to assess in future works how this superplasticity correlates with an alteration in the grain boundaries, plasticity and defect concentration of flash-sintered WC grains.

Funding

This work was partially supported within the program Departments of Excellence 2018–2022 (DII-UNITN "E-Mat") – funded by the Italian Ministry of University and Research (MIUR).

Declaration of Competing Interest

The authors declare that they have no known competing financial interests or personal relationships that could have appeared to influence the work reported in this paper.

Supplementary materials

Supplementary material associated with this article can be found, in the online version, at doi:10.1016/j.actamat.2023.119227.

Reference

[1] J. García, V. Collado Ciprés, A. Blomqvist, B. Kaplan, Cemented carbide microstructures: a review, Int. J. Refract. Metals. Hard. Mater 80 (2019) 40–68, https://doi.org/10.1016/j.ijrmhm.2018.12.004.

[2] Z. Roulon, J.M. Missiaen, S. Lay, Carbide grain growth in cemented carbides sintered with alternative binders, Int. J. Refract. Metals. Hard. Mater. 86 (2020), 105088, https://doi.org/10.1016/j.ijrmhm.2019.105088.

[3] H. Tripathy, C. Sudha, V.T. Paul, R. Thirumurugesan, T.N. Prasanthi, R. Sundar, N. Vijayashanthi, P. Parameswaran, S. Raju, High temperature thermophysical properties of spark plasma sintered tungsten carbide, Int. J. Refract. Metals. Hard. Mater 104 (2022), 105804, https://doi.org/10.1016/j.ijrmhm.2022.105804.

[4] T. Dash, B.B. Nayak, M. Abhangi, R. Makwana, S. Vala, S. Jakhar, C.V.S. Rao, T. K. Basu, Preparation and neutronic studies of tungsten carbide composite, Fus. Sci. Technol 65 (2014) 241–247, https://doi.org/10.13182/FST13-663.

[5] S.A. Humphry-Baker, G.D.W. Smith, Shielding materials in the compact spherical tokamak, Philosoph. Trans. Royal. Soc. A. Math. Phys. Eng. Sci. 377 (2019), 20170443, https://doi.org/10.1098/rsta.2017.0443.

[6] E.M. Garcia-Ayala, S. Tarancon, B. Ferrari, J.Y. Pastor, A.J. Sanchez-Herencia, Thermomechanical behaviour of WC-W2C composites at first wall in fusion conditions, Int. J. Refract. Metals. Hard. Mater. 98 (2021), 105565, https://doi.org/10.1016/j.ijrmhm.2021.105565.

[7] S.A. Humphry-Baker, G.D.W. Smith, G. Pintsuk, Thermal shock of tungsten carbide in plasma-facing conditions, J. Nucl. Mater. 524 (2019) 239–246, https://doi.org/10.1016/j.jnucmat.2019.06.041.

[8] J. Sun, J. Zhao, Z. Huang, K. Yan, X. Shen, J. Xing, Y. Gao, Y. Jian, H. Yang, B. Li, A review on binderless tungsten carbide: development and application, 2020. 10.1007/s40820-019-0346-1.

[9] P.A. Burr, S.X. Oliver, Formation and migration of point defects in tungsten carbide: unveiling the sluggish bulk self-diffusivity of WC, J. Eur. Ceram. Soc. 39 (2019) 165–172, https://doi.org/10.1016/j.jeurceramsoc.2018.10.001.

[10] K. Kornaus, M. Rączka, A. Gubernat, D. Zientara, Pressureless sintering of binderless tungsten carbide, J. Eur. Ceram. Soc. 37 (2017) 4567–4576, https://doi.org/10.1016/j.jeurceramsoc.2017.06.008.

[11] Y. Cheng, T. Zhu, J. Zhang, Y. Li, S. Sang, Z. Xie, Oscillatory pressure sintering of binderless tungsten carbide, Ceram. Int. 46 (2020) 25603–25607, https://doi.org/10.1016/j.ceramint.2020.07.033.

[12] J. Poetschke, V. Richter, A. Michaelis, Fundamentals of sintering nanoscaled binderless hardmetals, Int. J. Refract. Metals. Hard. Mater. 49 (2015) 124–132, https://doi.org/10.1016/j.ijrmhm.2014.04.022.

[13] E.A. Lantsev, N.V. Malekhonova, V.N. Chuvil'Deev, A.V. Nokhrin, M.S. Boldin, P. V. Andreev, K.E. Smetanina, Effect of initial particle size and various composition on the spark plasma sintering of binderless tungsten carbide, J. Phys. Conf. Ser. (2021) 1758, https://doi.org/10.1088/1742-6596/1758/1/012022.

[14] J. Zhao, T. Holland, C. Unuvar, Z.A. Munir, Sparking plasma sintering of nanometric tungsten carbide, Int. J. Refract. Metals. Hard. Mater. 27 (2009) 130–139, https://doi.org/10.1016/j.ijrmhm.2008.06.004.

[15] E.A. Lantsev, N.V. Malekhonova, V.N. Chuvil'Deev, A.V. Nokhrin, Y. V. Blagoveshchenskii, N.V. Isaeva, M.S. Boldin, P.V. Andreev, K.E. Smetanina, Binderless tungsten carbides with an increased oxygen content obtained by spark plasma sintering, J. Phys. Conf. Ser (2021) 1758, https://doi.org/10.1088/1742-6596/1758/1/012023.

[16] E. Lantsev, N. Malekhonova, A. Nokhrin, V. Chuvil'deev, M. Boldin, Y. Blagoveshchenskiy, P. Andreev, K. Smetanina, N. Isaeva, S. Shotin, Influence of oxygen on densification kinetics of WC nanopowders during SPS, Ceram. Int 47 (2021) 4294–4309, https://doi.org/10.1016/j.ceramint.2020.09.272.

[17] V.N. Chuvil'deev, Y.V. Blagoveshchenskiy, A.V. Nokhrin, M.S. Boldin, N. V. Sakharov, N.V. Isaeva, S.V. Shotin, O.A. Belkin, A.A. Popov, E.S. Smirnova, E. A. Lantsev, Spark plasma sintering of tungsten carbide nanopowders obtained through DC arc plasma synthesis, J. Alloys. Compd 708 (2017) 547–561, https://doi.org/10.1016/j.jallcom.2017.03.035.

[18] R.O. Ritchie, The conflicts between strength and toughness, Nat. Mater 10 (2011) 817–822, https://doi.org/10.1038/nmat3115.

[19] J. Sun, Y. Chen, J. Zhao, Nano-ceramic replacing cobalt in cemented carbide as binder phase: is it feasible? J. Alloys. Compd 896 (2022), 162968 https://doi.org/10.1016/j.jallcom.2021.162968.

[20] A. Kundu, J. Ma, J. Carrete, G.K.H. Madsen, W. Li, Anomalously large lattice thermal conductivity in metallic tungsten carbide and its origin in the electronic structure, Mater. Today. Phys 13 (2020), 100214, https://doi.org/10.1016/j.mtphys.2020.100214.

[21] A. Gubernat, P. Rutkowski, G. Grabowski, D. Zientara, Hot pressing of tungsten carbide with and without sintering additives, Int. J. Refract. Metals. Hard. Mater 43 (2014) 193–199, https://doi.org/10.1016/j.ijrmhm.2013.12.002.

[22] B. Yaman, H. Mandal, Spark plasma sintering of Co-WC cubic boron nitride composites, Mater. Lett 63 (2009) 1041–1043, https://doi.org/10.1016/j.matlet.2009.01.086.

[23] L.T. da Silva Soffner, A.A.A. dos Santos, R. da Silva Guimaraes, C.S. de Carvalho, M.E. Soffner, M.G. de Azevedo, M. Filgueira, Novel binder for NbC-based cemented carbides prepared by spark plasma sintering, Int. J. Refract. Metals. Hard. Mater 106 (2022), https://doi.org/10.1016/j.ijrmhm.2022.105864.

[24] X.L. Phuah, J. Cho, T. Tsakalakos, A.K. Mukherjee, H. Wang, X. Zhang, Defects in flash-sintered ceramics and their effects on mechanical properties, MRS. Bull 46 (2021) 44–51, https://doi.org/10.1557/s43577-020-00014-y.

[25] H. Motomura, D. Tamao, K. Nambu, H. Masuda, H. Yoshida, Athermal effect of flash event on high-temperature plastic deformation in Y2O3-stabilized tetragonal ZrO2 polycrystal, J. Eur. Ceram. Soc 42 (2022) 5045–5052, https://doi.org/10.1016/j.jeurceramsoc.2022.04.055.

[26] M.S. Tarasova, B.A. Tarasov, I.I. Konovalov, The role of plastic flow in processes of high-speed sintering of ceramic materials under pressure, KnE. Mater. Sci 4 (2018) 498, https://doi.org/10.18502/kms.v4i1.2203.

[27] B. Yang, Z. Shang, J. Li, X.L. Phuah, J. Cho, H. Wang, X. Zhang, Effects of electric field on microstructure evolution and defect formation in flash-sintered TiO2, J. Eur. Ceram. Soc 42 (2022) 6040–6047, https://doi.org/10.1016/j.jeurceramsoc.2022.06.009.
[28] D.M. Evans, D.R. Småbråten, T.S. Holstad, P.E. Vullum, A.B. Mosberg, Z. Yan, E. Bourret, A.T.J. Van Helvoort, S.M. Selbach, D. Meier, Observation of electric-field-induced structural dislocations in a ferroelectric oxide, Nano. Lett 21 (2021) 3386–3392, https://doi.org/10.1021/acs.nanolett.0c04816.
[29] J. Cho, Q. Li, H. Wang, Z. Fan, J. Li, S. Xue, K.S.N. Vikrant, H. Wang, T.B. Holland, A.K. Mukherjee, R.E. García, X. Zhang, High temperature deformability of ductile flash-sintered ceramics via in-situ compression, Nat. Commun 9 (2018) 1–9, https://doi.org/10.1038/s41467-018-04333-2.
[30] J. Cho, J. Li, H. Wang, Q. Li, Z. Fan, A.K. Mukherjee, W. Rheinheimer, H. Wang, X. Zhang, Study of deformation mechanisms in flash-sintered yttria-stabilized zirconia by in-situ micromechanical testing at elevated temperatures, Mater. Res. Lett 7 (2019) 194–202, https://doi.org/10.1080/21663831.2019.1575924.
[31] J. Li, J. Cho, J. Ding, H. Charalambous, S. Xue, H. Wang, X.L. Phuah, J. Jian, X. Wang, C. Ophus, T. Tsakalakos, R.Edwin García, A.K. Mukherjee, N. Bernstein, C.Stephen Hellberg, H. Wang, X. Zhang, Nanoscale stacking fault–assisted room temperature plasticity in flash-sintered TiO2, Sci. Adv 5 (2019) 1–10, https://doi.org/10.1126/sciadv.aaw5519.
[32] W. Rheinheimer, X.L. Phuah, H. Wang, F. Lemke, M.J. Hoffmann, H. Wang, The role of point defects and defect gradients in flash sintering of perovskite oxides, Acta. Mater 165 (2019) 398–408, https://doi.org/10.1016/j.actamat.2018.12.007.
[33] B. Qu, D. Eiteneer, L.A. Hughes, J. Preusker, J. Wood, W. Rheinheimer, M. J. Hoffmann, K. van Benthem, Defect redistribution along grain boundaries in SrTiO3 by externally applied electric fields, J. Eur. Ceram. Soc (2022), https://doi.org/10.1016/j.jeurceramsoc.2022.11.028.
[34] X. Fang, K. Ding, S. Janocha, C. Minnert, W. Rheinheimer, T. Frömling, K. Durst, A. Nakamura, J. Rödel, Nanoscale to microscale reversal in room-temperature plasticity in SrTiO3 by tuning defect concentration, Scr. Mater 188 (2020) 228–232, https://doi.org/10.1016/j.scriptamat.2020.07.033.
[35] S. Stich, K. Ding, Q.K. Muhammad, L. Porz, C. Minnert, W. Rheinheimer, K. Durst, J. Rödel, T. Frömling, X. Fang, Room-temperature dislocation plasticity in SrTiO 3 tuned by defect chemistry, J Am. Ceram. Soc 105 (2022) 1318–1329, https://doi.org/10.1111/jace.18118.
[36] I. Mazo, L.E. Vanzetti, J.M. Molina-Aldareguia, A. Molinari, V.M. Sglavo, Role of surface carbon nanolayer on the activation of flash sintering in tungsten carbide, Int. J. Refract. Metals. Hard. Mater (2022), 106090, https://doi.org/10.1016/j.ijrmhm.2022.106090.
[37] I. Mazo, A. Molinari, V.M. Sglavo, Electrical resistance flash sintering of tungsten carbide, Mater. Des 213 (2022), 110330, https://doi.org/10.1016/j.matdes.2021.110330.
[38] I. Mazo, A. Molinari, V.M. Sglavo, Effect of pressure on the electrical resistance flash sintering of tungsten carbide, J. Eur. Ceram. Soc 42 (2022) 2028–2038, https://doi.org/10.1016/j.jeurceramsoc.2022.01.017.
[39] B.D. Cullity, S.R. Stock, Elements of X-Ray Diffraction, Third Edit, PEARSON, 2014. www.pearsoned.co.uk.
[40] A.S. Kurlov, A.I. Gusev, Tungsten carbides and W-C phase diagram, Inorg. Mater. 42 (2006) 121–127, https://doi.org/10.1134/S0020168506020051.
[41] R. Raj, Joule heating during flash-sintering, J. Eur. Ceram. Soc 32 (2012) 2293–2301, https://doi.org/10.1016/j.jeurceramsoc.2012.02.030.
[42] M.N. Rahaman, Sintering of Ceramics, CRC Press, 2007, https://doi.org/10.1201/b15869-2.
[43] H. Jelitto, G.A. Schneider, A geometric model for the fracture toughness of porous materials, Acta. Mater 151 (2018) 443–453, https://doi.org/10.1016/j.actamat.2018.03.018.
[44] H. Jones, V. Tong, R. Ramachandramoorthy, K. Mingard, J. Michler, M. Gee, Micropillar compression of single crystal tungsten carbide, Part 1: temperature and orientation dependence of deformation behaviour, Int. J. Refract. Metals. Hard. Mater 102 (2022), 105729, https://doi.org/10.1016/j.ijrmhm.2021.105729.
[45] H. Taimatsu, S. Sugiyama, Y. Kodaira, Synthesis of W2C by reactive hot pressing and its mechanical properties, Mater. Trans 49 (2008) 1256–1261, https://doi.org/10.2320/matertrans.MRA2007304.
[46] X. Liu, J. Zhang, C. Hou, H. Wang, X. Song, Z. Nie, Mechanisms of WC plastic deformation in cemented carbide, Mater. Des 150 (2018) 154–164, https://doi.org/10.1016/j.matdes.2018.04.025.
[47] V. Tong, H. Jones, K. Mingard, Micropillar compression of single crystal tungsten carbide, part 2: lattice rotation axis to identify deformation slip mechanisms, Int. J. Refract. Metals. Hard. Mater 103 (2022), https://doi.org/10.1016/j.ijrmhm.2021.105734.
[48] F.R.N. Nabarro, S.B. Luyckx, U.V. Waghmare, Slip in tungsten monocarbide. I. Some experimental observations, Mater. Sci. Eng. A 483–484 (2008) 139–142, https://doi.org/10.1016/j.msea.2006.09.153.
[49] F.R.N. Nabarro, S.B. Luyckx, U.V. Waghmare, Slip in tungsten monocarbide. II. A first-principles study, Mater. Sci. Eng. A 483–484 (2008) 9–12, https://doi.org/10.1016/j.msea.2006.09.174.
[50] F. De Luca, H. Zhang, K. Mingard, M. Stewart, B.M. Jablon, C. Trager-Cowan, M. G. Gee, Nanomechanical behaviour of individual phases in wc-co cemented carbides, from ambient to high temperature, Materialia. (Oxf) 12 (2020), https://doi.org/10.1016/j.mtla.2020.100713.
[51] M. Lee, High temperature hardness of tungsten carbide, Metall. Trans. A 14 (1983) 1625–1629, https://doi.org/10.1007/BF02654390.
[52] F. Wakai, N. Kondo, Y. Shinoda, Ceramics superplasticity, Curr. Opin. Solid. State. Mater. Sci. 4 (1999) 461–465, https://doi.org/10.1016/S1359-0286(99)00053-4.
[53] J.S.C. Francis, R. Raj, Flash-sinterforging of nanograin zirconia: field assisted sintering and superplasticity, J. Am. Ceram. Soc 95 (2012) 138–146, https://doi.org/10.1111/j.1551-2916.2011.04855.x.
[54] F. Wakai, N. Kondo, H. Ogawa, T. Nagano, S. Tsurekawa, Ceramics superplasticity: deformation mechanisms and microstructures, Mater. Charact 37 (1996) 331–341, https://doi.org/10.1016/S1044-5803(96)00174-X.
[55] G. Pezzotti, K. Ota, Grain-boundary sliding in fluorine-doped silicon nitride, J. Am. Ceram. Soc 80 (1997) 599–603, https://doi.org/10.1111/j.1151-2916.1997.tb02873.x.
[56] J.M. Lebrun, C.S. Hellberg, S.K. Jha, W.M. Kriven, A. Steveson, K.C. Seymour, N. Bernstein, S.C. Erwin, R. Raj, In-situ measurements of lattice expansion related to defect generation during flash sintering, J. Am. Ceram. Soc 100 (2017) 4965–4970, https://doi.org/10.1111/jace.15071.
[57] H. Charalambous, S.K. Jha, K.S.N. Vikrant, R.E. García, X.L. Phuah, H. Wang, H. Wang, A. Mukherjee, T. Tsakalakos, Electric field-induced grain boundary degradation mechanism in yttria stabilized zirconia, Scr. Mater 204 (2021), 114130, https://doi.org/10.1016/j.scriptamat.2021.114130.
[58] M. Biesuz, V.M. Sglavo, Current-induced abnormal and oriented grain growth in corundum upon flash sintering, Scr. Mater 150 (2018) 82–86, https://doi.org/10.1016/j.scriptamat.2018.03.004.
[59] W. Ji, J. Zhang, W. Wang, Z. Fu, R. Todd, The microstructural origin of rapid densification in 3YSZ during ultra-fast firing with or without an electric field, J. Eur. Ceram. Soc 40 (2020) 5829–5836, https://doi.org/10.1016/j.jeurceramsoc.2020.07.027.
[60] J. Narayan, Grain growth model for electric field-assisted processing and flash sintering of materials, Scr. Mater 68 (2013) 785–788, https://doi.org/10.1016/j.scriptamat.2013.01.008.